# Chapter-6

Blank page

# 6. Influence of oleic acid-treated $LaF_3$ nanoparticles as an additive on extreme pressure properties of various grades of polyalphaolefins using four-ball tribometer

*This chapter explains the extreme pressure characteristics of different grades of polyalphaolefins (i.e., PAO 4, PAO 6, PAO 40, and PAO 100) with $LaF_3$ nanoparticles as an additive. The $LaF_3$ nanoparticles were synthesized by the sol-gel method and modified with oleic acid. Tribological test results revealed the role of nanoadditive on the lubrication performance of PAO oils.*

## 6.1. Characterization of oleic acid modified $LaF_3$ nanoparticles

**Figure 6.1(a)** depicts the X-ray diffractometer (XRD) pattern of synthesized OA-modified $LaF_3$ nanoparticles. The profile exhibits the principal diffraction peaks at 24.4˚, 27.6˚, 34.9˚, 43.6˚, 44.8˚, 50.5˚, 52.6˚, 64.1˚, 67.8˚, 70.4˚, 80.7˚, and 85.3˚, which corresponds to the characteristic diffractions plane of (110), (111), (112), (300), (113), (302), (221), (223), (115), (411), (413) and (332), respectively [78]. All the peaks correspond to JCPDS reference code 00-008-0461, which is related to the hexagonal structure phase of $LaF_3$. Meanwhile, no other phases were identified, indicating that the surface modification does not cause changes in the crystal structure of $LaF_3$ [79].

The presence of functional groups was determined with the aid of Fourier transform infrared spectroscopy (FTIR), and the recorded spectrum of OA-$LaF_3$ nanoparticles is shown in **Figure 6.1(b)**. A broad absorption peak that appeared at 3418 $cm^{-1}$ is assigned to the stretching vibration of the O-H group originated from the adsorbed water [159]. The two peaks that emerged at 2925 $cm^{-1}$ and 2853 $cm^{-1}$ are ascribed to the asymmetric and symmetric C-H stretching vibrations of -$CH_3$ and -$CH_2$, respectively. Moreover, a peak at 1412 $cm^{-1}$ is attributed to the C-H deformation vibrations of -$CH_2$ [160]. The above result

demonstrated the successful introduction of long alkyl chains into the OA-LaF3 nanoparticles. The peaks obtained at 1584 $cm^{-1}$ and 1082 $cm^{-1}$ are due to the C-O stretching of the carboxylic group [161,162]. As a result, it is reasonable to assume that during the synthesis of the OA-$LaF_3$ nanoparticles, a chemical reaction between oleic acid and the $LaF_3$ nanocores occurred. Furthermore, a peak spotted at 591 $cm^{-1}$ corresponds to the characteristic stretching vibration of the La-F bond [79]. Therefore, the above findings validate that the $LaF_3$ nanoparticles were successfully modified by oleic acid.

**Figures 6.1(c)-6.1(d)** display the high-resolution scanning electron microscope (HR-SEM) and high-resolution transmission electron microscopy (HR-TEM) images of OA-$LaF_3$ nanoparticles, respectively. It can be observed that the OA-$LaF_3$ nanoparticles revealed the morphology of approximately spherical. The nanoparticles as-formed are not uniform in diameter. The TEM image of OA-$LaF_3$ nanoparticles (**Figure 6.1(d)**) exhibits no apparent evidence of agglomeration. This implies that the dispersion stability of $LaF_3$ nanoparticles is significantly increased and effectively prevented from agglomeration after being surface modified by oleic acid. The diameters of $LaF_3$ nanoparticles were calculated with the aid of IMAGE J software. The variation in the diameter of $LaF_3$ with the number of counts is presented in **Figure 6.1(e)**. The mean diameter of the nanoparticles was determined to be ~15 nm, and the diameter distribution was between 5 nm to 36 nm. **Figure 6.1(f)** shows the size vs. frequency distribution of $LaF_3$ nanoparticles, and the majority of the nanoparticles were in the range of 5-25 nm.

X-ray photoelectron spectroscopy (XPS) was adopted to get better insights into the chemical states of the constituent elements present in OA-$LaF_3$ nanoparticles and the binding energy associated with different chemical bonds and related compounds**. Figure 6.2(a)** displays the XPS survey spectra of all elements identified in OA-$LaF_3$ nanoparticles. In contrast, the deconvoluted spectrum of individual elements (i.e., C 1s, La 3d, F 1s, and

O 1s) is shown in **Figures 6.2(b)-6.2(e)**. The core-level spectra of C 1s (Figure 6.2(b) exhibits three peaks with binding energies 284.27, 286.72, and 287.23 eV. The peak with binding energy 284.1 eV could be ascribed to adventitious carbon at the surface of the $LaF_3$ nanoparticles. The other peaks at 286.72 and 287.23 eV are assigned to C-O and O-C=O or C-F bonds, respectively [163]. **Figure 6.2(c)** shows the La 3d spectrum with four peaks at 837.87, 839.25, 854.18, and 857.21 eV. The two peaks at 837.87 and 839.25 eV are ascribed to the La $3d_{5/2}$ and indicate the La-F bond, whereas La 3d is located at 854.18 and 857.21 eV assigned to La $3d_{3/2}$ [164]. The spectra of F 1s (**Figure 6.2(d)**) can be deconvoluted into two peaks at 684.54 and 687.47 eV, indicating atomic F ions in different chemical environments. Moreover, the La $3d_{5/2}$ peak at 837.87 eV in coalition with the F 1s peak at 684.54 eV validates that La exists in the La (III) state, i.e., $LaF_3$ [162]. **Figure 6.2(e)** depicts the high-resolution spectrum of O 1s. The two peaks at bonding energies of 531.47 eV and 533.80 eV could be ascribed to $O^2$ species [165]. The lower binding energy component at 528.13 eV is attributed to La-O bonds, and the peak at 530 eV is allocated to the hydroxyl group due to the adsorbed moisture from the air [166].

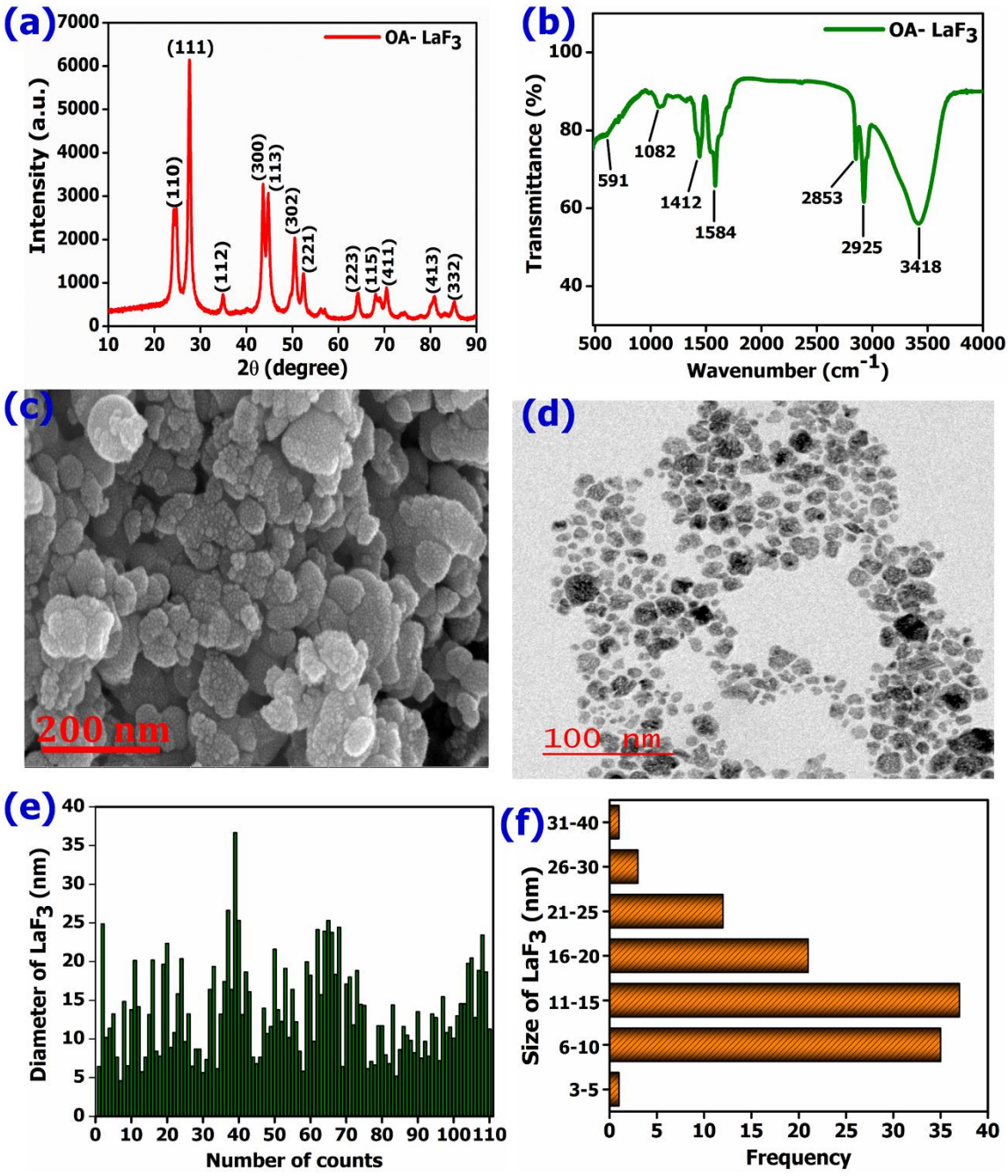


**Figure 6.1:** (a) XRD pattern, (b) FTIR spectra, (c) FE-SEM micrograph, (d) HR-TEM image of $LaF_3$ nanoparticles, (e) variation in the diameter of $LaF_3$, and (f) size and frequency distribution of nanoparticles

.

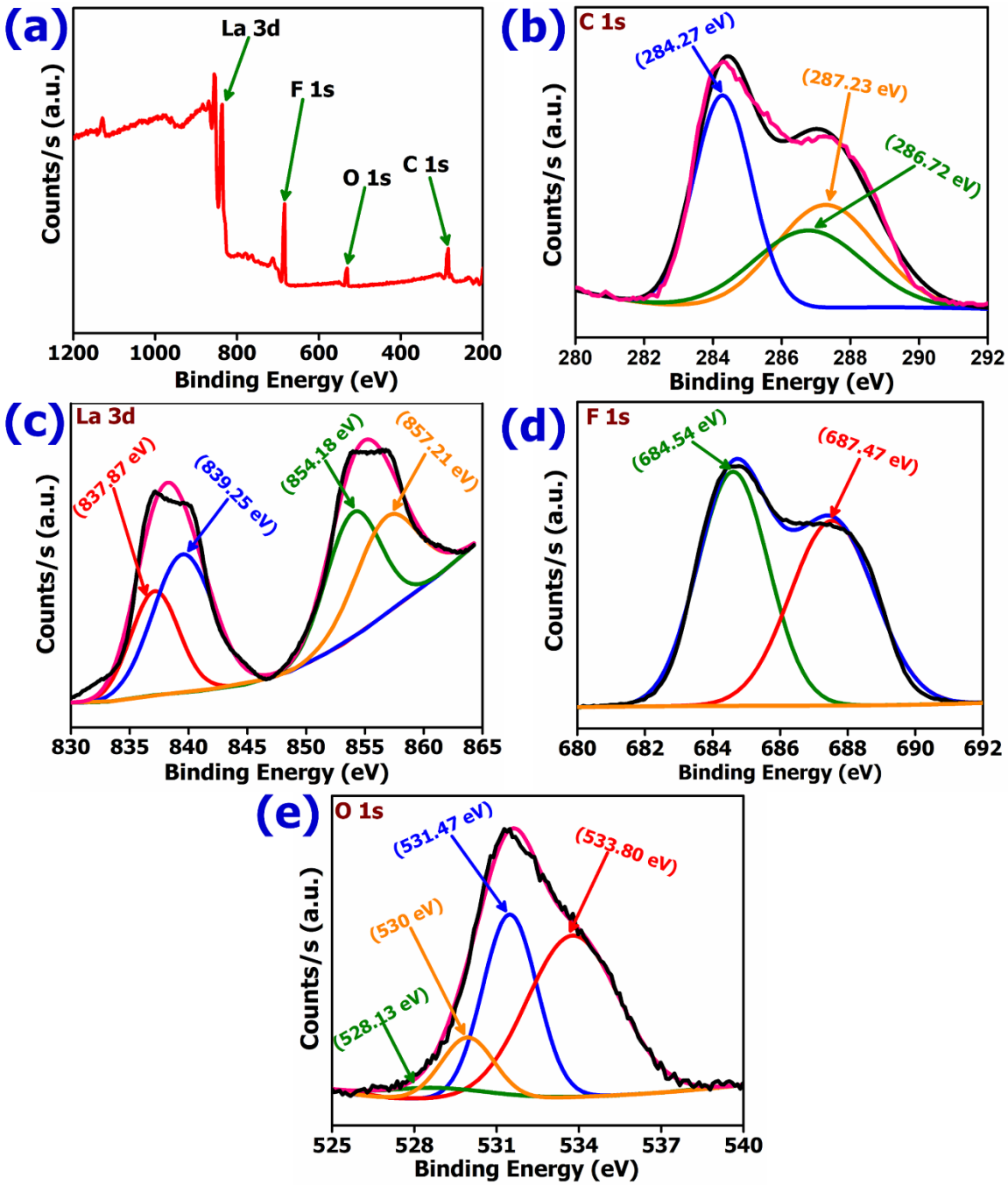


**Figure 6.2:** (a) XPS survey spectra of $LaF_3$ nanoparticles, and corresponding deconvoluted XPS spectra of (b) C 1s, (c) La 3d, (d) F 1s, and (e) O 1s

## 6.2. Tribological performance of nanolubricants under EP conditions

### 6.2.1. EP properties of low viscosity PAOs-based nanolubricants (PAO 4 and PAO 6)

This test aims to evaluate the load-carrying properties of lubricating oils under high loads generally encountered in gears. The results of extreme pressure tests for low viscosity

PAOs-based nanolubricants are summarized in **Table 6.1**. Whereas, **Figure 6.3** demonstrates the variation in wear scar diameter (WSD) with applied load. Furthermore, the various parameters used in this study are illustrated in **Figure 6.3(a)**. It can be observed from **Figure 6.3(a)** and **Table 6.1** that all doses of $LaF_3$ in PAO 4 are unable to make an impact on the last non-seizure load (LNSL), initial seizure load (ISL), just before weld (JBWL), and weld load (WL). Although, the load wear index (LWI) of PAO 4 was improved with the inclusion of nanoparticles. The variation of diameter with applied load (**Figure 6.3(a)**) indicates that the WSD of PAO 4 suspension was decreased when the dose of $LaF_3$ increased from 0.025-0.15 wt.% compared to plain PAO 4 under all applied load. Consequently, the LWI of PAO 4 based nanolubricants increased, as shown in **Table 6.1**. The LWI of PAO 4 was increased approximately linearly as the concentration of additive increased from 0.025-0.15 wt.%. However, a mild decrease in LWI was identified at a concentration of 0.075 wt.% in PAO 4. However, it was less than plain PAO 4. In comparisons with plain PAO 4, at different concentrations (0.025-0.15 wt.%), PAO 4 showed an increment in LWI around 1 to 13%. Thus, PAO 4 +0.15 wt.% $LaF_3$ suspension exhibited the best anti-wear performance (i.e., lowest WSD at ISL and JBWL and higher LWI) under extreme pressure conditions, as listed in **Table 6.1**. The identical behaviour of $LaF_3$ was also obtained in the case of PAO 6-based nanolubricants (as displayed in **Figure 6.3(b)** and **Table 6.1)**, except the LNSL and ISL were increased from 392 to 491 N and 491 to 618 N, respectively, when $LaF_3$ were dispersed in plain PAO 6. Furthermore, PAO 6 at all doses of additive showed a similar value of LNSL and ISL. Although the LWI of PAO 6 was improved at all additive concentrations (0.025-0.15 wt.%), the increment in LWI was in the range of 24-30% compared to plain PAO 6. But JBWL and WL retained the same values as for plain PAO 6. But JBWL and WL retained the same values as for plain PAO 6. In contrast and exceptionally, the WSD at ISL and JBWL were decreased

significantly compared to plain PAO 6 as the doses of $LaF_3$ increased from 0.025-0.15 wt.% as displayed in **Table 6.1**. Therefore, 0.15 wt.% was the optimum dose in PAO 6, which demonstrated the best EP behaviour. The above results referred that the wear behaviour of both plain PAOs was almost identical in terms of LNSL, ISL, JBWL, WSD at ISL, and JBWL as well as WL. The same trend of variation in the parameters was identified for both PAO-based nanolubricants with different additive doses. Nevertheless, PAO 6-based nanolubricants demonstrated better EP properties than PAO 4-based nanolubricants (**Table 6.1**). The possible rationale is that PAO 6 featured better viscous characteristics (i.e., higher VI and higher viscosity) than PAO 4, as shown in **Table 3.1**, leading to the development of relatively thick film thickness between the interfaces mating surfaces. Moreover, the wear behaviour of both PAO-based nanolubricants was similar to plain PAOs below the ISL (Figure 6.3). These results appear to be related to the short test duration, and also these experiments were performed in the anti-wear region (region below ISL). However, different effects can be observed at ISL.

### 6.2.2. EP properties of high viscosity PAOs-based nanolubricants (PAO 40 and PAO 100)

**Figure 6.4(a)** depicts the change in the WSD with varied loads for plain PAO 40 and PAO 40 with various doses of $LaF_3$, whereas the EP properties are listed in **Table 6.2**. It can be noticed from **Figure 6.4(a)** and **Table 6.2** that for plain PAO 40, LNSL, ISL, JBWL, and WL were observed to be 618 N, 785 N, 1236 N, and 1570N, respectively. When 0.025wt.% of $LaF_3$ was added into PAO 40, there was no improvement in the aforementioned parameters, but the immense rise in WSD at ISL was recognized. As a result, LWI was decreased from 625 to 566 N compared to plain PAO 40 (**Table 6.2**). Further increasing the doses from 0.05 to 0.075 wt.%, PAO 40 showed the amelioration in LNSL and ISL. However, JBWL and WL managed the same value as for plain PAO 40. It can also be

observed from **Figure 6.4(a)** and **Table 6.2** that PAO 40 incorporating 0.1-0.15 wt.% $LaF_3$ revealed the enhancement in WSD, JBWL, and WL. Whereas the value of LNSL and ISL remains the same as that of PAO 40, containing 0.05-0.075 wt.% of $LaF_3$. In the EP region (i.e., the region above LNSL), the pressures and temperature are very high, and generally, lubricants are squeezed out under high loading conditions. In this situation, the efficacy of additives in base oils plays a role, and the additives are supposed to withstand these extremities. $LaF_3$ owing to the hexagonal crystal structure, good resistance to thermal attack, and high melting point, could form a barrier between friction pairs sustaining extremities to enhance the WL. PAO 40 incorporating 0.15 wt.% offered the highest LWI and lowest WSD at ISL and JBWL and exhibited the maximum augmentation in LWI, approximately 13%. It was noticed from **Figure 6.4(b)** and **Table 6.2** that plain PAO 100 featured improvements in LNSL (785 N), ISL (981 N), JBWL (1570 N), WL (1962), and LWI (693 N) compared to plain PAO 40. The PAO 100 shows high viscosity characteristics that form lubricant film that can sustain under high loading conditions. On the other hand, the inclusion of 0.025 wt. % $LaF_3$ in PAO 100 attenuated the LNSL and ISL but exhibited lower WSD at ISL and JBWL than PAO 40, containing 0.025 wt.% $LaF_3$. Further, increase in the concentration of $LaF_3$ up to 0.15 wt.% in PAO 100, the values of LNSL and ISL were identical to plain PAO 100. Although, WL was increased to 2453 N when 0.15 wt. % dose of additive was dispersed in PAO 100. Therefore, 0.15 wt.% of $LaF_3$ in PAO 100 was the optimum concentration that produced the best EP properties. Overall, PAO 100-based nanolubricants demonstrated the best EP characteristics (i.e., higher LWI, higher WL, and minimum wear scar at ISL and JBWL) than PAO 40-based nanolubricants.

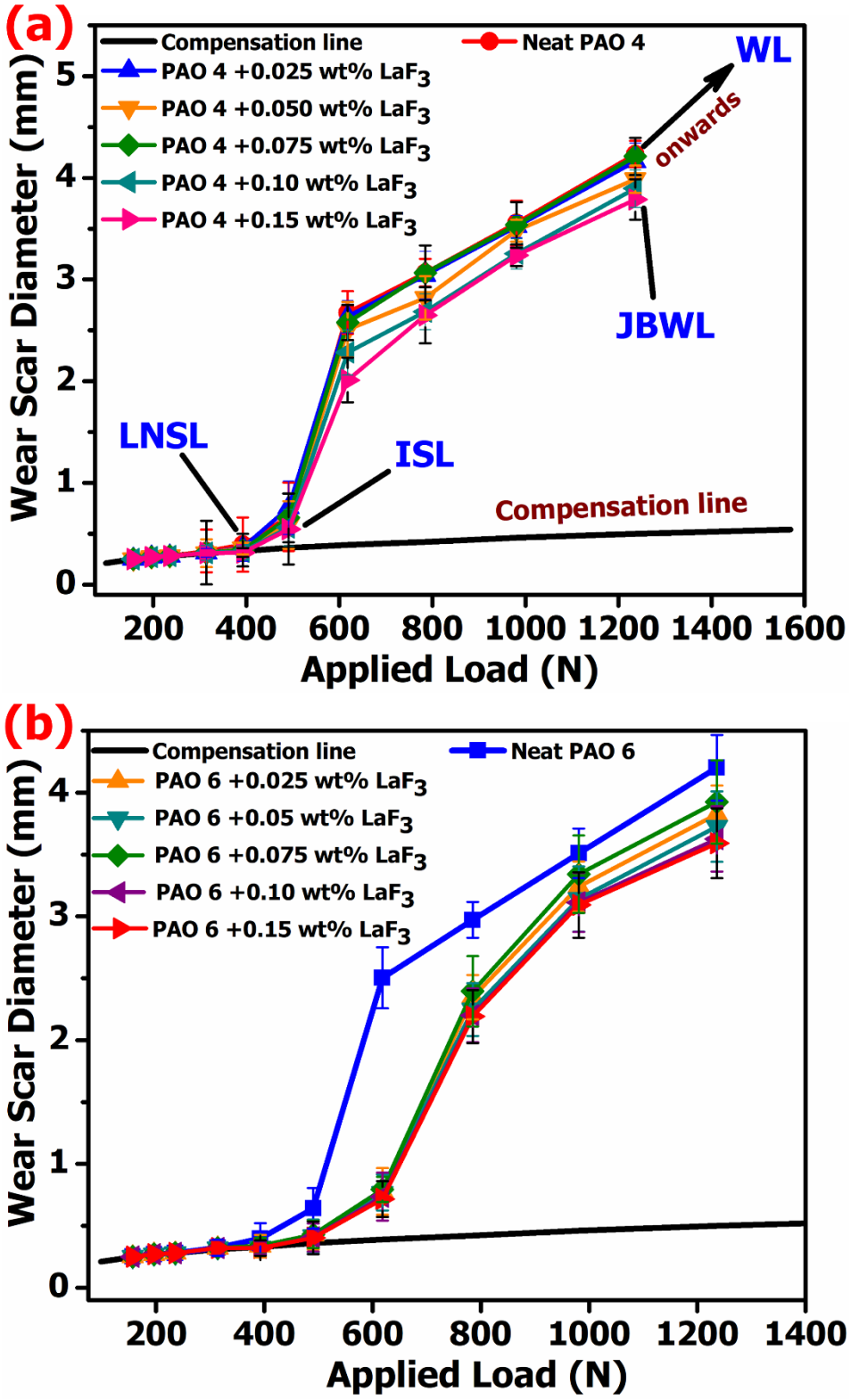


**Figure 6.3:** Variation in the wear scar diameter of worn surfaces lubricated by (a) PAO 4, and (b) PAO 6-based nanolubricants with applied load

**Table 6.1:** Summary of EP properties of PAO 4 and PAO 6 at different concentrations of $LaF_3$ nanoparticles

| Tribological parameters | Base oil | Concentration of $LaF_3$ nanoparticles (wt.%) in PAOs | | | | | |
|---|---|---|---|---|---|---|---|
| | | 0 | 0.025 | 0.05 | 0.075 | 0.1 | 0.15 |
| Last non seizure load (LNSL), (N) | PAO 4 | 392 | 392 | 392 | 392 | 392 | 392 |
| | PAO 6 | 392 | 491 | 491 | 491 | 491 | 491 |
| Initial seizure load (ISL), (N) | PAO 4 | 491 | 491 | 491 | 491 | 491 | 491 |
| | PAO 6 | 491 | 618 | 618 | 618 | 618 | 618 |
| Mean scar diameter at ISL, (mm) | PAO 4 | 0.67 | 0.64 | 0.59 | 0.66 | 0.56 | 0.55 |
| | PAO 6 | 0.64 | 0.78 | 0.77 | 0.79 | 0.74 | 0.72 |
| Just before weld load (JBWL), (N) | PAO 4 | 1236 | 1236 | 1236 | 1236 | 1236 | 1236 |
| | PAO 6 | 1236 | 1236 | 1236 | 1236 | 1236 | 1236 |
| Mean wear scar diameter at JBWL (mm) | PAO 4 | 4.235 | 4.162 | 3.987 | 4.211 | 3.896 | 3.787 |
| | PAO 6 | 4.202 | 3.825 | 3.726 | 3.924 | 3.625 | 3.591 |
| Weld load, (N) | PAO 4 | 1570 | 1570 | 1570 | 1570 | 1570 | 1570 |
| | PAO 6 | 1570 | 1570 | 1570 | 1570 | 1570 | 1570 |
| Load wear index (LWI), (N) | PAO 4 | 372 | 375 | 395 | 387 | 409 | 417 |
| | PAO 6 | 377 | 466 | 474 | 462 | 482 | 490 |

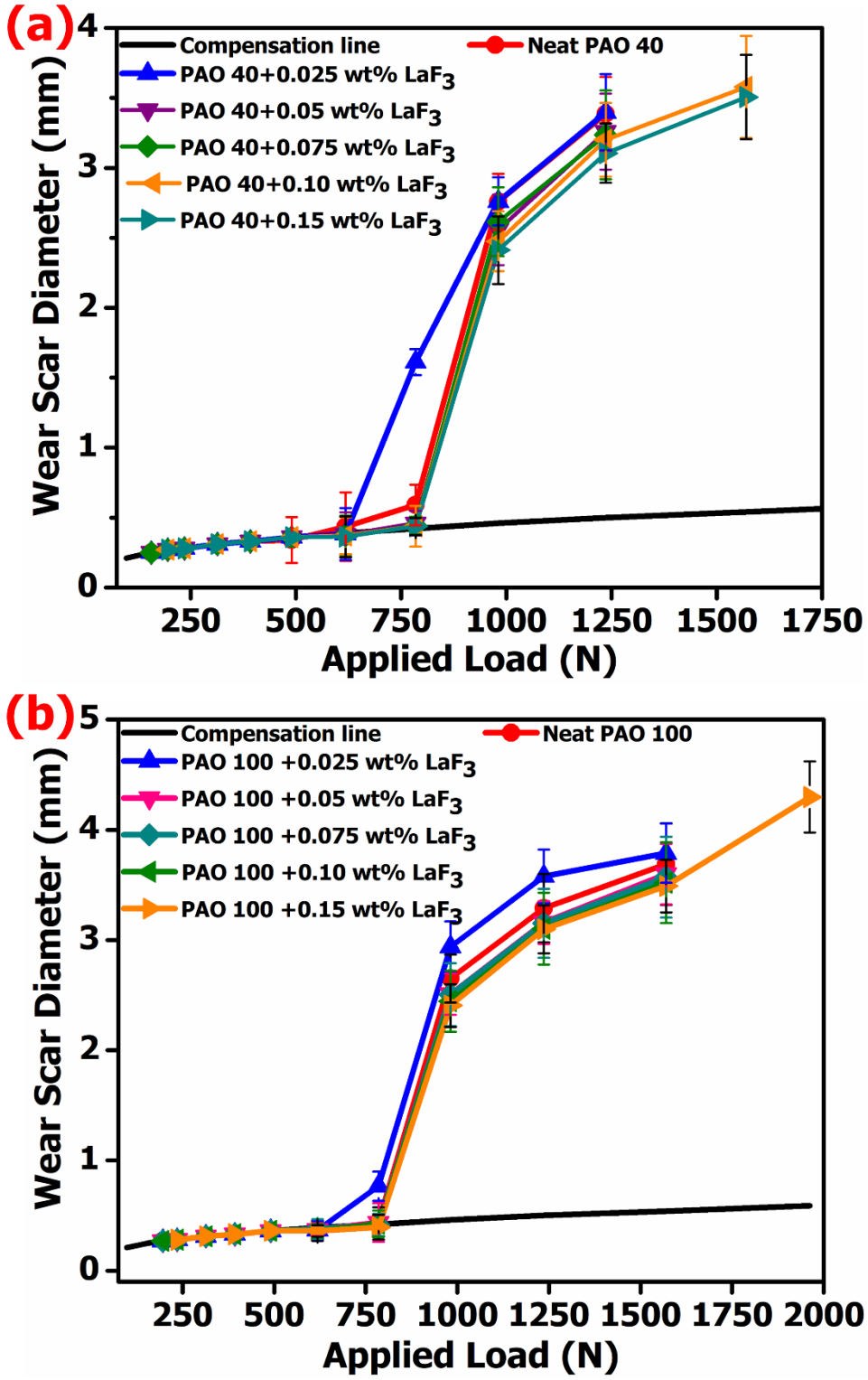


**Figure 6.4:** Wear scar diameter as a function of applied load (a) PAO 40, and (b) PAO 100-based nanolubricants

**Table 6.2:** Outline of EP properties of PAO 40 and PAO 100-based nanolubricants

| Tribological parameter | Base oil | Concentration of $LaF_3$ nanoparticles (wt.%) in PAOs | | | | | |
|---|---|---|---|---|---|---|---|
| | | 0 | 0.025 | 0.05 | 0.075 | 0.1 | 0.15 |
| Last non seizure load (LNSL), (N) | PAO 40 | 618 | 618 | 785 | 785 | 785 | 785 |
| | PAO 100 | 785 | 618 | 785 | 785 | 785 | 785 |
| Initial seizure load (ISL), (N) | PAO 40 | 785 | 785 | 981 | 981 | 981 | 981 |
| | PAO 100 | 981 | 785 | 981 | 981 | 981 | 981 |
| Mean scar diameter at ISL, (mm) | PAO 40 | 0.59 | 1.61 | 2.55 | 2.61 | 2.47 | 2.41 |
| | PAO 100 | 2.65 | 0.77 | 2.51 | 2.50 | 2.44 | 2.40 |
| Just before weld load (JBWL), (N) | PAO 40 | 1236 | 1236 | 1236 | 1236 | 1570 | 1570 |
| | PAO 100 | 1570 | 1570 | 1570 | 1570 | 1570 | 1962 |
| Mean wear scar diameter at JBWL (mm) | PAO 40 | 3.386 | 3.398 | 3.258 | 3.236 | 3.579 | 3.506 |
| | PAO 100 | 3.689 | 3.788 | 3.599 | 3.571 | 3.521 | 4.297 |
| Weld load, (N) | PAO 40 | 1570 | 1570 | 1570 | 1570 | 1962 | 1962 |
| | PAO 100 | 1962 | 1962 | 1962 | 1962 | 1962 | 2453 |
| Load wear index (LWI), (N) | PAO 40 | 625 | 566 | 670 | 677 | 696 | 701 |
| | PAO 100 | 693 | 622 | 695 | 701 | 705 | 731 |

## 6.3. Analysis of worn surfaces

### 6.3.1. SEM analysis of worn surfaces

To understand the wear mechanisms of the worn steel balls, the SEM was used for the analysis, and the results are depicted in **Figures 6.5-6.6**. The first column in both figures exhibits the low magnification micrographs revealing WSD formed on steel balls. In contrast, higher magnification micrographs (i.e., in the second column) are used to quantify the intensity of wear. A larger wear scar with typical plastic deformation zones with wide grooves and scratches were identified on the worn surface, suggesting abrasive and adhesive wear with plain PAO 4 as shown in **Figures 6.5(a)-6.5(b)**. This might be due to continuous formation and decomposition of the lubricating film under higher loading conditions (785 N), which leads to plucking/chipping off or surface-originated spalling of ball material. However, despite higher loading conditions, lower wear scar with shallower groves (milder damage) and relatively smoother surfaces was found when lubricated by PAO 4 containing 0.15 wt.% $LaF_3$ (**Figures 6.5(c)-6.5(d)**). This might be ascribed to the deposition and self-repairing function of $LaF_3$ on the matting surface. The extent of surface smoothness varied due to the difference in the contribution of $LaF_3$ and PAO oil molecules towards film formation. The worn surface of the steel balls tested with plain PAO 6 (**Figures 6.5(e)-6.5(f)**) unveiled signs of ploughing action and the formation of micro-grooves with an adequate amount of spalling and rough wear scar. Although, the magnitude of wear scar was comparable to worn surface lubricated by plain PAO 4 (**Figures 6.5(a)-6.5(b)**). The severity of wear was further mitigated when 0.15 wt.% $LaF_3$ was added in PAO 6 as displayed in **Figures 6.5(g)-6.5(h)**, and the worn surface appears to be wrapped by a protective layer, resulting in improvement in EP properties as reported in **Table 6.1**.

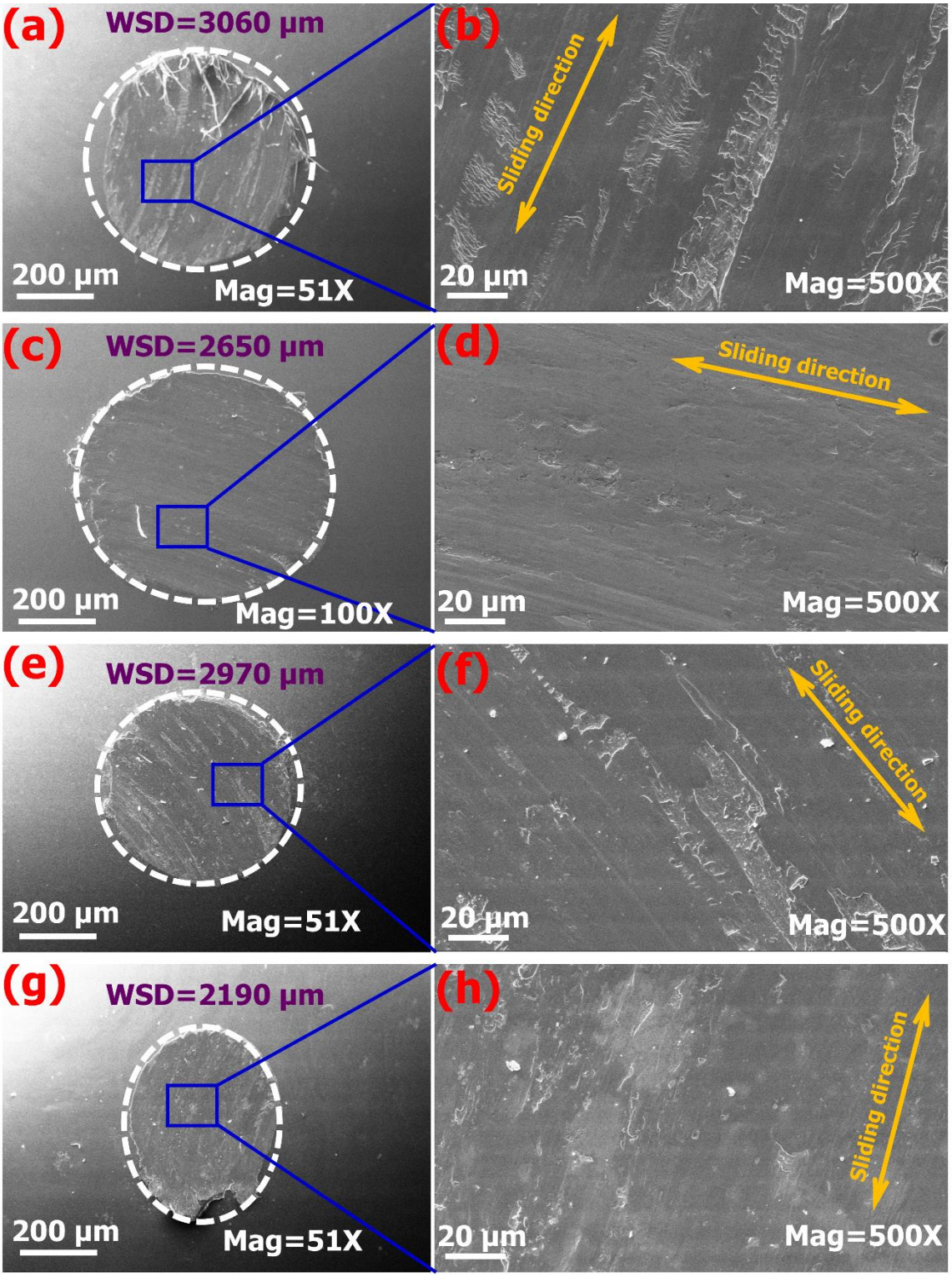


**Figure 6.5:** Worn surfaces of steel balls lubricated with (a, b) plain PAO 4; (c, d) PAO 4 containing 0.15 wt.% $LaF_3$; (e, f) plain PAO 6, and (g, h) PAO 6 containing 0.15 wt.% $LaF_3$. (Applied load: 785 N and test duration: 10 s)

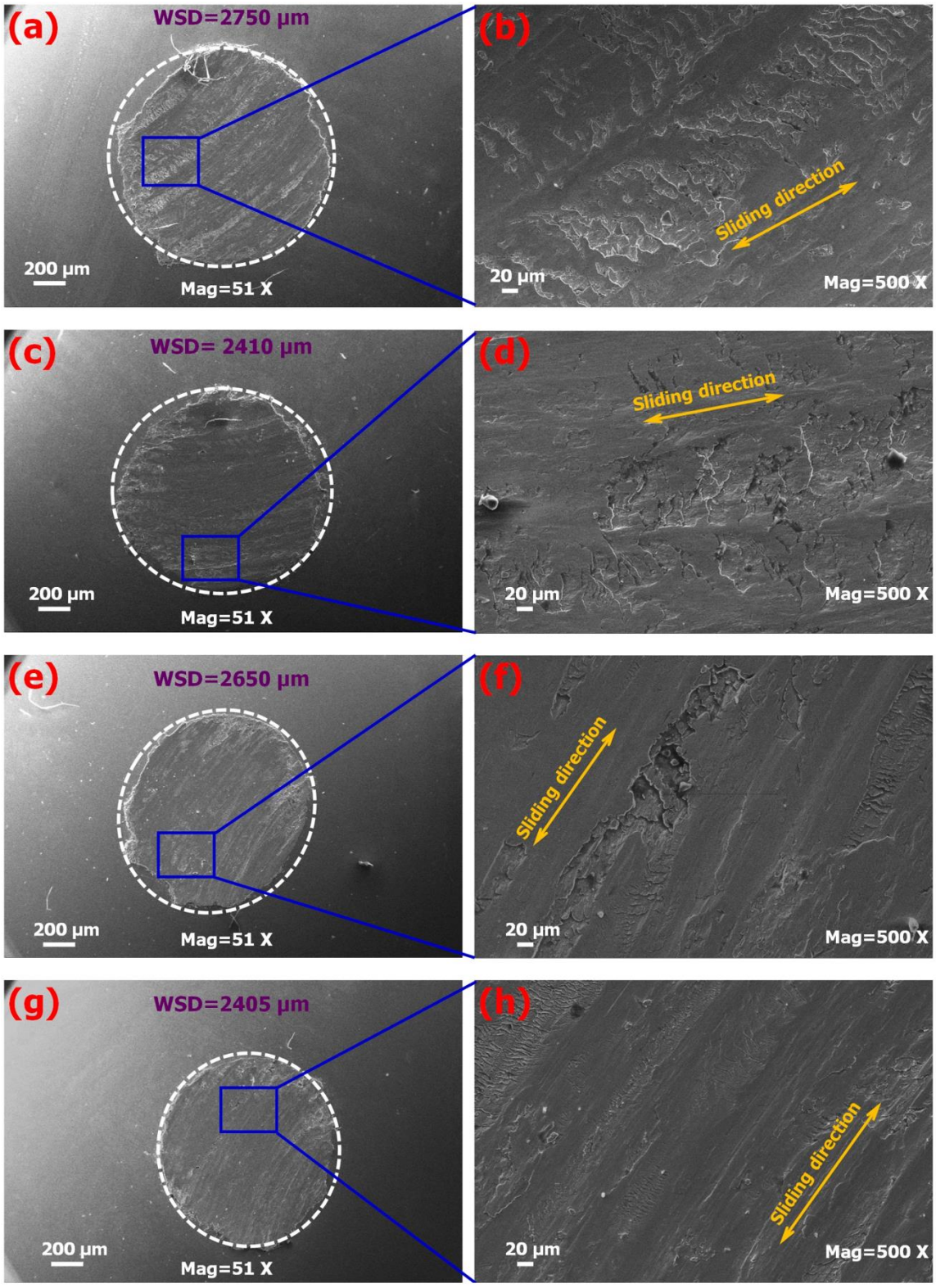


**Figure 6.6:** Worn surfaces of steel balls lubricated by (a, b) plain PAO 40; (c, d) PAO 40 containing 0.15 wt.% $LaF_3$; (e, f) plain PAO 100; (g, h) PAO 100 containing 0.15 wt.% $LaF_3$. (Applied load: 981 N and test duration: 10 s)

**Figure 6.6** represents the SEM micrograph of worn surfaces lubricated by high viscosity PAOs-based nanolubricants. The clear characteristics of severe thermal fatigue cracks along with chipped-off material at several places appeared under the lubrication of plain PAO 40 (**Figures 6.6(a)-6.6(b)**). This might be ascribed to the application of high load (981N). However, a significantly lower wear scar was noticed than the surface lubricated by plain PAO 4 and PAO 6 (**Figure 6.5**). It can also be observed that worn surface lubricated by PAO 40 incorporating 0.15 wt.% $LaF_3$ (**Figures 6.6(c)-6.6(d)**) evidenced a smaller scar and relatively smooth surface with mild ploughing and some amount of residual wear debris along the friction direction. The smallest wear scar and smoothest worn surfaces were obtained in the case of PAO 100 containing 0.15 wt.% $LaF_3$ as shown in **Figures 6.6(g)-6.6(h)**. The results showed that the inclusion of $LaF_3$ nanoparticles in PAO oils produced the mending effect by filling the grooves of frictional surfaces and forming robust protecting tribo-film on the interface of matting pairs. Therefore, the smoothening of the friction surfaces **(Figures 6.6(g)-6.6(h)**), also the EP results in **Figure 6.4(b)** and **Table 6.2** manifested the positive contribution of $LaF_3$ nanoparticles on enhancing the EP properties.

### 6.3.2. Surface topography analysis of worn steel balls by SPM

The surface topography in 2 D and 3 D micrographs of worn surfaces of tested steel balls lubricated by plain PAOs and PAOs containing $LaF_3$ nanoparticles are shown in **Figures 6.7-6.8**, and corresponding roughness values of worn surfaces are summarized in **Table 6.3**. The 3D micrographs of worn surfaces lubricated by plain PAOs (**Figures 6.7(b), 6.7(f) and Figures 6.8(b), 6.8(f)**) demonstrated deep micro-ploughing marks by the asperities. In contrast, the 3D micrographs of the worn surfaces experimented with PAOs containing $LaF_3$ nanoparticles revealed comparably polished surfaces with a minimum number of furrows and abrasion marks over the contact interface (**Figures 6.7(d), 6.7(h)**) and **Figures**

**6.8(d), 6.8(h)**). The 2D micrographs of worn surface lubricated by PAOs containing $LaF_3$ (**Figures 6.7 and 6.8**) signified better distribution of green and yellow contours representing a relatively low friction area than worn surfaces lubricated by plain PAOs (i.e., yellow and green contour). **Figures 6.7(d), 6.7(h)** and **Figures 6.8(d), 6.8(h)** exhibited the tribo-sintering of nanoparticles in the micro-grooves due to shearing, which resulted in considerable enhancement in EP properties. The surface roughness ($S_q$) values were undergone enormous reduction when $LaF_3$ nanoparticles were dispersed in all PAO oils. As expected, minimum surface roughness and smoothest surface were obtained when tested with PAO 100 containing 0.15 wt.% of $LaF_3$ as displayed in Table 6.3, also corroborated by SEM results (**Figures 6.5-6.6**).

For a better conception of the peaks, valleys, and their respective distribution on worn surfaces, bearing area ratio (BAR) curves were plotted for steel balls lubricated with plain PAOs, and PAOs containing $LaF_3$ are displayed in **Figure 6.9**. Meanwhile, the values of several roughness parameters which were extracted from the BAR curve (i.e., $S_k$, $S_{pk}$, $S_{vk}$, $S_{r1}$, $S_{r2}$) and from the 2D roughness profile (i.e., $S_{sk}$, $S_{ku}$, $\Delta_a$, $\Delta_q$) are specified in **Table 6.3**. The representation of all symbols used in the BAR curve is illustrated in **Figure 6.9(a)**. The upper fragment of the BAR curve is denoted as reduced peak height ($S_{pk}$), which is generally worn out during the running-in period. The middle region is expressed as the core zone ($S_k$) that sustains the load during the stable period and affects the longevity of the components. The lower segment of the curve is called reduced valley depth ($S_{vk}$) which functions as a lubricant reservoir. The parameters $S_{r1}$ and $S_{r2}$ represent the percentage of bearing area ratio found in the limits of the core profile. It can be observed from **Figure 6.9** and **Table 6.3** that a significant reduction in $S_k$, $S_{pk}$ and $S_{r1}$ were obtained in the case of PAOs containing $LaF_3$. This implied that peaks on the worn surface were polished off, which led to flattening the middle region of its BAR curve. Therefore, smooth surfaces

were obtained and shown in SEM and SPM micrographs (**Figures 6.5-6.6** and **Figures 6.7-6.8**). In contrast, the $S_{vk}$ and $S_{r2}$ values of worn surfaces (**Figure 6.9(b, d, f, and h**) were increased than plain PAOs, which illustrates the good retention capacity of nanolubricants in the micro valleys of rubbing surfaces. Furthermore, it can also be noticed from **Table 6.3** that the worn surface lubricated by PAOs containing $LaF_3$ nanoparticles, $S_k$, $S_{pk}$ and $S_{r1}$ were decreased with a decrease in surface roughness, while $S_{vk}$ and $S_{r2}$ were increased with a reduction in the surface roughness. It was reported that the percentage of valleys remained more or less or the same with a reduction in surface roughness [167].

Since surface roughness is an important characteristic and directly influences functionality, such as wear and fatigue performance. But the surface roughness alone may not be enough to predict surface performance, depending on many other geometric parameters, such as skewness ($S_{sk}$) and kurtosis ($S_{ku}$). The skewness of topography height distribution measures the asymmetry of surface deviations about the mean plane. The $S_{sk}$ for an asymmetric distribution of topography heights can be negative if the distribution has more valleys or positive if the distribution has more peaks[168]. The worn surfaces lubricated by plain PAOs showed a negative value of $S_{sk}$ indicating more valleys on worn surfaces as displayed in SPM images (**Figures 6.7-6.8**). Whereas, $S_{sk}$ of worn surfaces lubricated by PAOs containing $LaF_3$ were positive, implying that $LaF_3$ nanoparticles were deposited in the valleys and produced relatively smooth surfaces with peaks rather than valleys. The kurtosis ($S_{ku}$) is denoted as a measure of peakiness of height distribution about the mean line. The distribution curve with a lower value ($S_{ku} < 3$) is regarded as a platykurtic surface, with low peaks and valleys. The distribution curve acquiring a higher value ($S_{ku} > 3$) is called leptokurtic demonstrating a spiky surface [169]. Therefore, all worn surfaces owing $S_{ku} < 3$ (as shown in Table 6.3) are labelled as platykurtic surfaces. Although, worn

surfaces lubricated by PAOs containing $LaF_3$ nanoparticles exhibited an increased value of $S_{ku}$ than plain PAOs (i.e., a similar trend as observed in the case of $S_{sk}$).

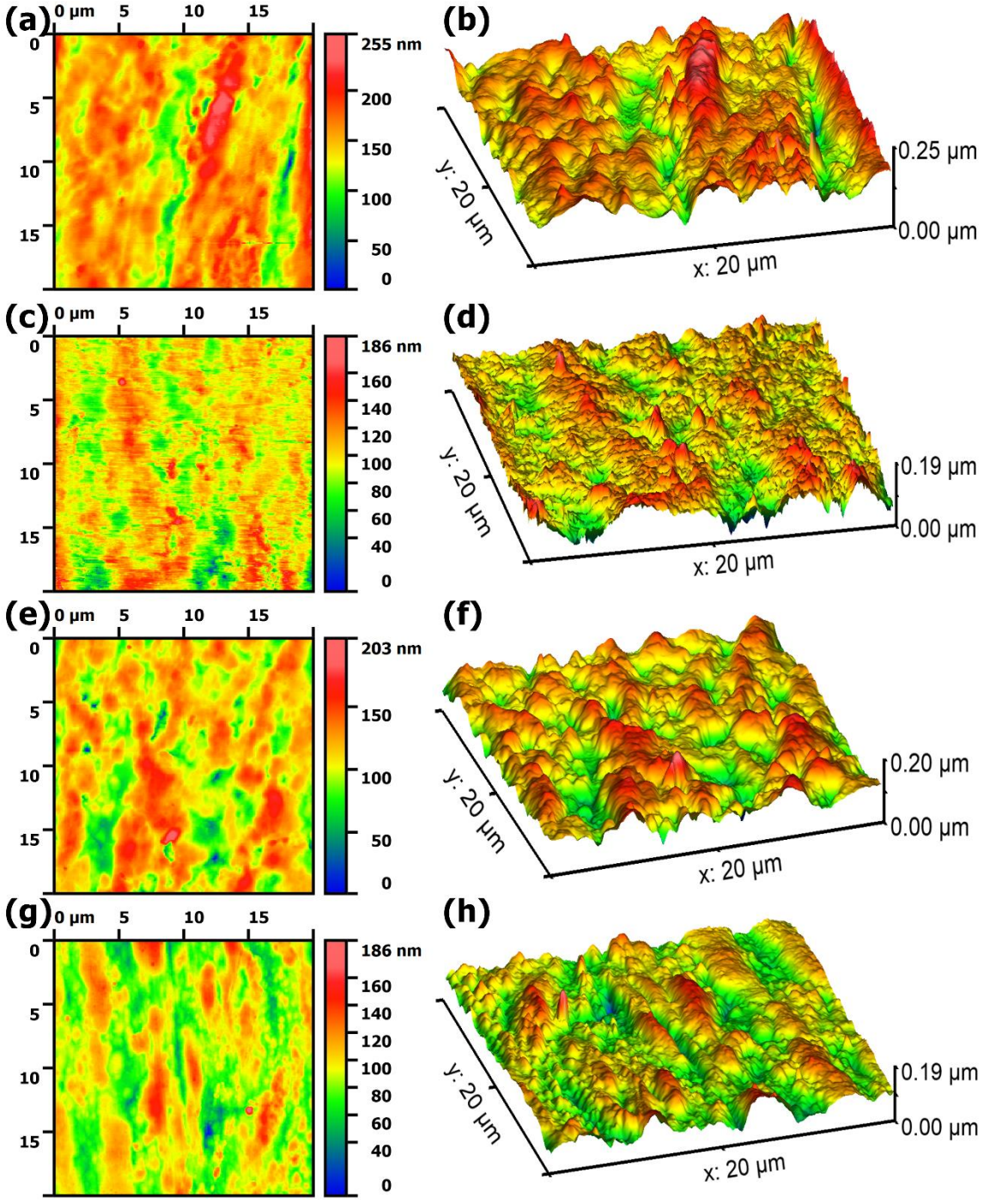


**Figure 6.7:** Topographic micrographs of steel balls experimented with (a, b) plain PAO 4; (c, d) PAO 4 containing 0.15 wt.% $LaF_3$; (e, f) plain PAO 6, and (g, h) PAO 6 containing 0.15 wt.% $LaF_3$ (Note: a, c, e, and g: top view and b, d, f, and h: three-dimensional view of worn surfaces). (Applied load: 785 N and test duration: 10 s)

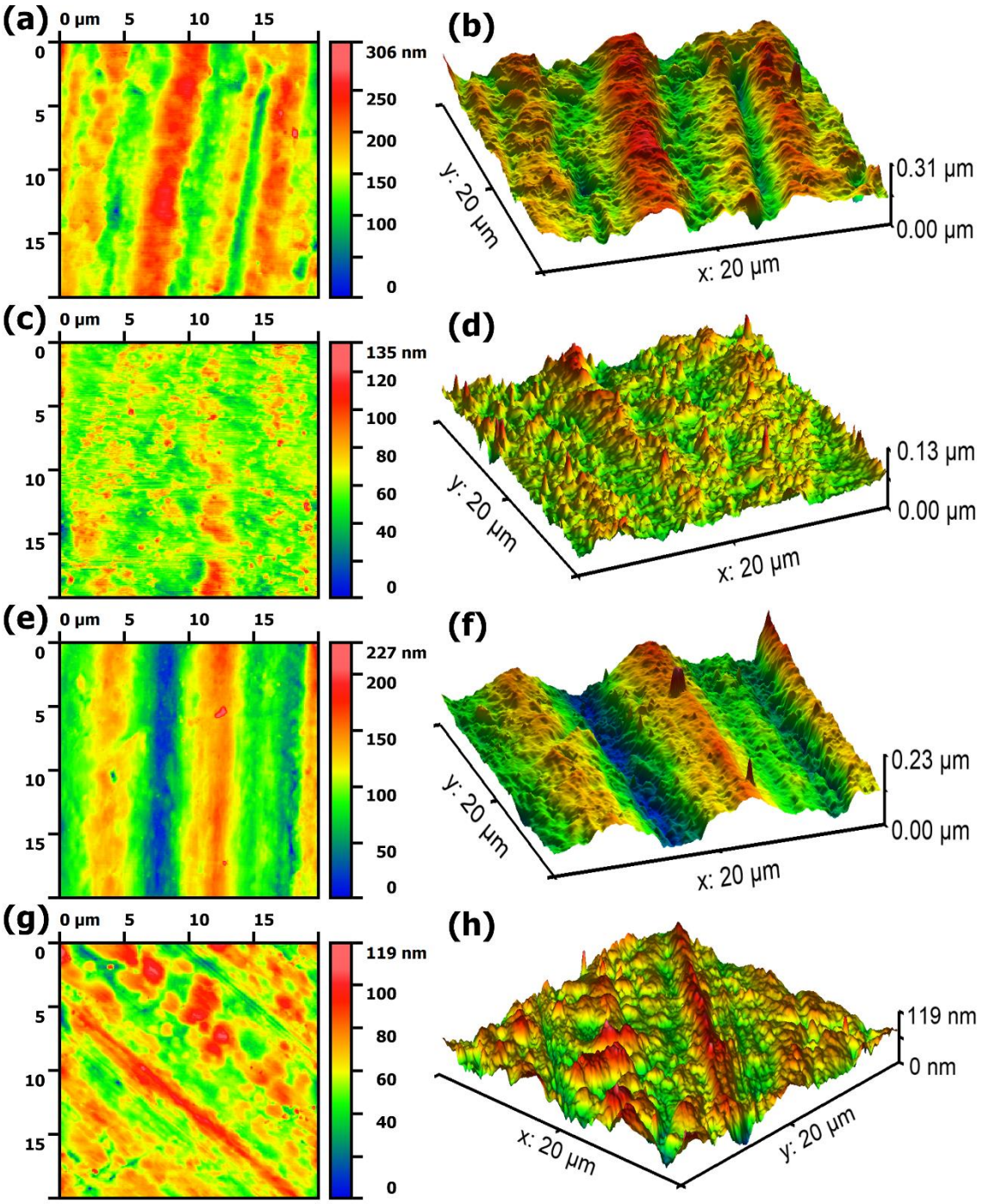


**Figure 6.8:** Topographic micrographs of steel balls experimented with (a, b) plain PAO 40; (c, d) PAO 40 containing 0.15 wt.% $LaF_3$; (e, f) plain PAO 100, and (g, h) PAO 100 containing 0.15 wt.% $LaF_3$ (Note: a, c, e, and g: top view and b, d, f, and h: three-dimensional view of worn surfaces). (Applied load: 981 N and test duration: 10 s)

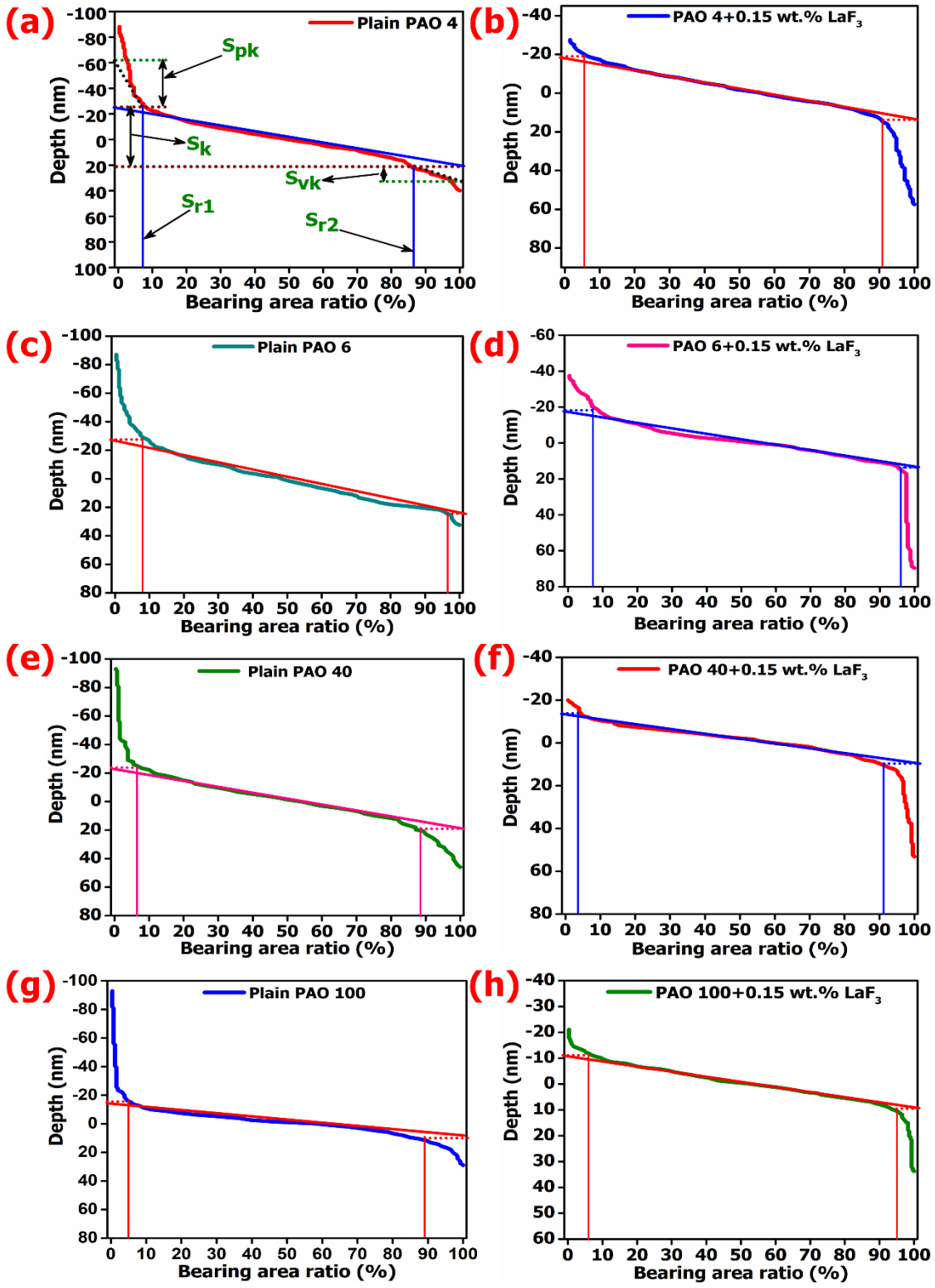


**Figure 6.9:** Bearing area ratio (BAR) curves of steel balls lubricated with different lubricant compositions. (Applied load: 785 N for low viscosity PAOs and 981 N for high viscosity PAOs based nanolubricants, and test duration: 10 s)

**Table 6.3:** Surface roughness parameter of worn steel balls tested with various lubricant formulations

| Lubricant composition | Surface roughness | | Amplitude parameter | | Morphological parameter | | | | | Hybrid parameter | |
|---|---|---|---|---|---|---|---|---|---|---|---|
| | $S_a$ (nm) | $S_q$ (nm) | $S_{sk}$ | $S_{ku}$ | $S_k$ (nm) | $S_{pk}$ (nm) | $S_{vk}$ (nm) | $S_{r1}$ (%) | $S_{r2}$ (%) | $\Delta_a$ | $\Delta_q$ |
| **Plain PAO 4** | 21.8 | 28.1 | -0.074 | 0.612 | 46.7 | 37.1 | 12.1 | 7.2 | 86.5 | 0.055 | 0.081 |
| **PAO 4+0.15 wt.% $LaF_3$** | 13.9 | 18.2 | -0.0381 | 0.875 | 32.8 | 9.1 | 32.5 | 5.6 | 90.8 | 0.046 | 0.069 |
| **Plain PAO 6** | 17.9 | 22.6 | -0.234 | 0.279 | 51.6 | 29.1 | 9.1 | 7.9 | 96.5 | 0.052 | 0.079 |
| **PAO 6+0.15 wt.% $LaF_3$** | 14.9 | 18.9 | 0.089 | 0.334 | 32.3 | 18.9 | 46.5 | 7.2 | 96.3 | 0.043 | 0.077 |
| **Plain PAO 40** | 30.3 | 37.6 | -0.253 | -0.256 | 42.9 | 36.4 | 24.2 | 6.6 | 88.6 | 0.051 | 0.076 |
| **PAO 40+0.15 wt.% $LaF_3$** | 14.9 | 19.1 | 0.167 | 0.189 | 23.4 | 8.1 | 34.1 | 3.6 | 91.4 | 0.033 | 0.054 |
| **Plain PAO 100** | 27.5 | 33.1 | -0.247 | -0.483 | 25.6 | 26.4 | 11.2 | 5.9 | 89.3 | 0.043 | 0.078 |
| **PAO 100+0.15 wt.% $LaF_3$** | 11.1 | 14.1 | 0.207 | 0.226 | 20.8 | 6.1 | 13.5 | 4.8 | 95.2 | 0.032 | 0.046 |

Hybrid parameters also play an essential role in surface engineering because they elucidate both characteristics of surfaces, i.e., vertical and spatial characteristics, and are generally adopted for quantifying wear in tribological applications [170]. The two-hybrid parameters, i.e., mean slope of profile ($\Delta_a$) and RMS slope of profile ($\Delta_q$), are used in this study, as shown in **Table 6.3**. Both factors may be influenced by various mechanical properties such as elastic contact, fatigue crack initiation, friction, and hydrodynamic lubrication. A higher value may reveal a peaky surface, whereas a lower value may signify a smoother surface. [171]. In addition, the RMS slope of the profile is notably affected by the sampling interval. It can be noticed from **Table 6.3** that worn surfaces lubricated by PAOs containing $LaF_3$ nanoparticles revealed lower values of $\Delta_a$ and $\Delta_q$ compared to plain PAOs. The lowest values of both parameters were obtained in the case of PAO 100 incorporating 0.15 wt.% $LaF_3$, suggesting the smoothest worn surface among all lubrication formulations, also manifested by SEM and SPM analysis (**Figures 6.5-6.8**).

### 6.3.3. EDS analysis of worn surfaces

EDS was used to identify the chemical constituents on the worn surfaces experimented with various lubricant formulations, and the results are arranged in **Figure 6.10**. It can be noticed from **Figure 6.10** that EDS spectra of worn surfaces lubricated by plain PAOs indicated the presence of Fe, C, Cr, and O. The elements, i.e., Fe, C, and Cr, may be due to steel ball material. Moreover, the presence of C on the worn surface may be due to the base oil (i.e., hydrocarbon degradation of olefins). The existence of O validates the formation of the oxide layer between the friction pairs when the iron is reacted to air. On the contrary, F and La along with Fe, C, Cr, O elements were identified on the worn surfaces lubricated by PAOs containing $LaF_3$, which illustrates that $LaF_3$ nanoparticles may accumulate in the nano grooves of rubbing surfaces to form tribo-film. Consequently, preventing direct metal-to-metal contact leads to improved EP properties (**Section 6.2**). Moreover, it is

straightforward to comprehend the development and decomposition of lubricating film at the interfaces of friction pairs. It was simultaneously happened during the boundary lubrication due to higher loading conditions. A noticeable EP performance could be attained when the speed of the film decomposition is less than the film formation [94].

## 6.4. Dispersion stability analysis of nanolubricants

Long-term dispersion stability of nanoparticles in the lubricating medium is one of the prerequisites for tribological applications. The dispersion stability of oleic acid-modified $LaF_3$ nanoparticles in all PAOs was evaluated at room temperature (~30℃) using visual monitoring through sediment photograph capturing over time, as depicted in **Figure 6.11**. In the present study, it is challenging to distinguish the sedimentation of $LaF_3$ in all PAOs due to exhibiting similar white colour in appearance. Therefore, the region of sedimentation is marked in the photographs. It can be observed from **Figure 6.11** that 0.025-0.075 wt.% of $LaF_3$ in PAO 4 revealed the initiation of sedimentation after 24 hours, and the phenomenon of precipitation continued for the observation done up to 15 days. In PAO 6, sedimentation was observed at two concentrations of synthesized nanoparticles (i.e., 0.025 and 0.05 wt.%). On the contrary, no macroscopic sediments were noticed in PAO 40 and PAO 100 at all doses of $LaF_3$, exhibiting good suspension stability even after 15 days (**Figures 6.11(i)- 6.11(p)**)

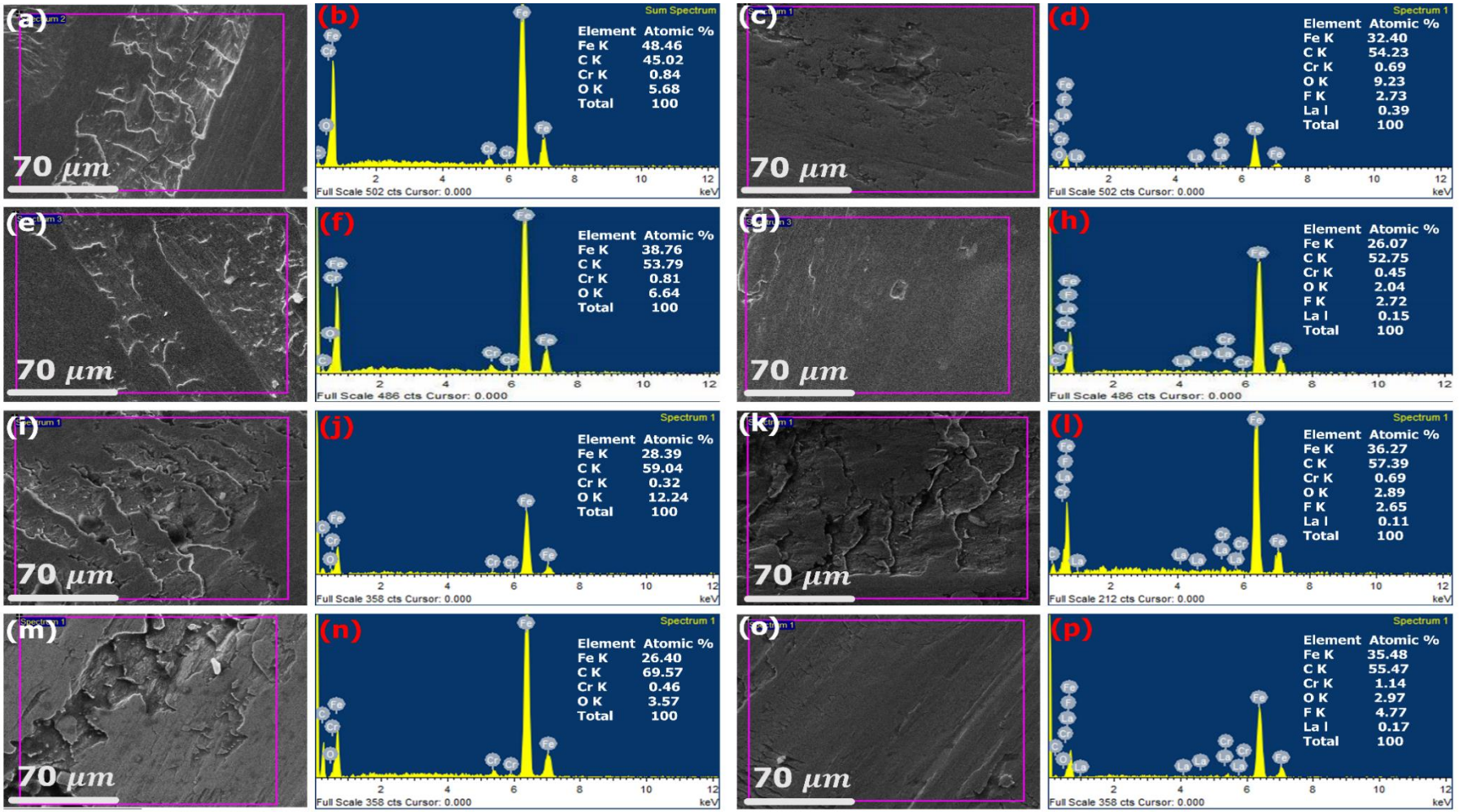


**Figure 6.10:** EDS spectrum of worn scars of steel balls lubricated with (a, b) plain PAO 4; (c, d) PAO 4 containing 0.15 wt.% $LaF_3$; (e, f) plain PAO 6; (g, h) PAO 6 containing 0.15 wt.% $LaF_3$; (i, j) plain PAO 40; (k, l) PAO 40 containing 0.15 wt.% $LaF_3$, and (m, n) plain PAO 100, and (o, p) PAO 100 containing 0.15 wt.% $LaF_3$. (Applied load: 785 N for low viscosity PAOs and 981 N for high viscosity PAOs based nanolubricants, and test duration: 10 s)

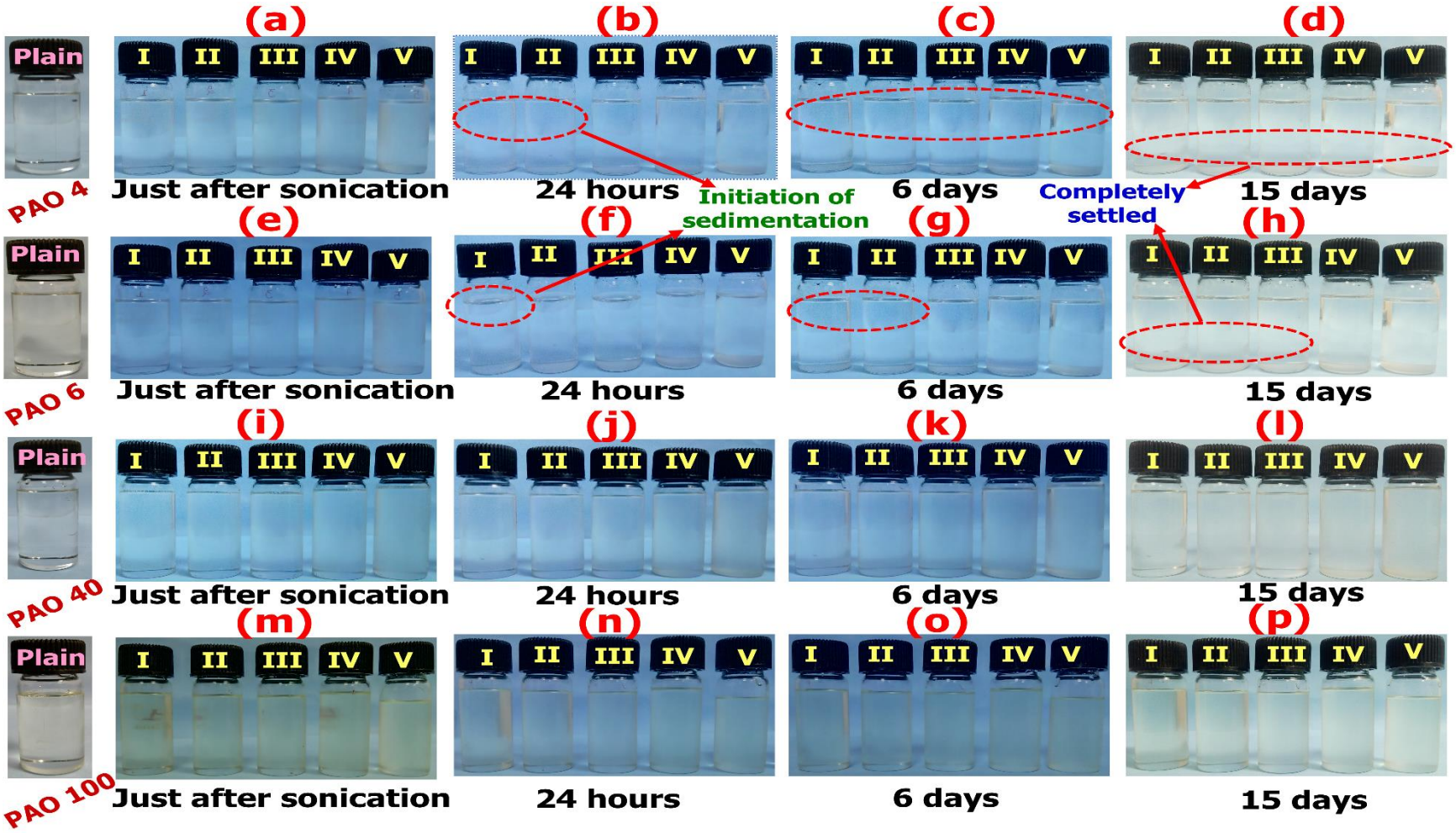


**Figure 6.11:** Photograph depicts the dispersion stability of $LaF_3$ at room temperature (~30°C) in (a-d) PAO 4; (e-h) PAO 6; (i-l) PAO 40, and (m-p) PAO 100 at different time interval

## 6.5. Rheological characterization of PAOs

To opt for a suitable lubricant for tribological applications, the rheological performance of lubricants plays an important role. All rheological characterizations were carried out only on plain PAOs. This study presumed that the inclusion of $LaF_3$ nanoparticles in all grades of PAO would not significantly affect the rheological characteristics because the doses of $LaF_3$ opted in this study were small (i.e., 0.025-0.15 wt.%). The primary purpose is to provide the rheological characterizations of plain PAOs to support the EP results (**Section 6.2**). **Figure 6.12(a)** shows the variation in shear stress as a function of shear rate at a temperature of 75℃. It can be observed from **Figure 6.12(a)** that the shear stress of all plain PAOs was increased with an increase in the shear rate. The maximum shear stress was offered by plain PAO 100 throughout the investigated range of shear rate except at lower shear rate (0.01-0.04 $S^{-1}$) and showing an approximately linear relationship with shear rate.

The same trend (variation of stress with shear rate) was also found in the case of plain PAO 40. Moreover, plain PAO 40 revealed the maximum shear stress at a lower shear rate. In contrast, PAO 6 demonstrated minimum shear stress at a low shear rate than plain PAO 4, PAO 40, and PAO 100. Still, the shear stress offered by PAO 6 became more dominant than PAO 4 at a higher shear rate and revealed a linear relationship with shear rate. The variation in dynamic viscosity of PAOs with varying shear rates is illustrated in **Figure 6.12(b)**. It can be ascertained that the dynamic viscosity of plain PAO 100 was declined continuously with an increase in the shear rate up to 0.15 $S^{-1}$, which demonstrated a non-Newtonian behaviour, i.e., exhibiting shear-thinning or pseudoplastic behaviour. Afterward, the viscosity continuously increased, followed by remained relatively constant as the shear rate increased from 0.07 to 100 $S^{-1}$, which signified the Newtonian behaviour of PAO 100. Compared to plain PAO 100, acquired a substantial reduction in the dynamic

viscosity of plain PAO 4, PAO 6, and PAO 40 with an increase in shear rate. However, it showed a limiting and constant value of viscosity at a higher-level shear rate. The constant viscosity at a higher shear rate means there is no chance of shear restructuring of fluid molecules at higher shear rates. Consequently, no effect of shear rate on the dynamic viscosity was identified. Since plain PAO 100 revealed the nominal diminution in viscosity with varying shear rates. Therefore, plain PAO 100 offered the best EP properties (as explained in **section 6.2**). On the other hand, the worst EP properties were obtained in plain PAO 4 due to maximum reduction in viscosity with shear rate.

Besides flow behaviour (shear-dependent dynamic viscosity properties), the viscoelasticity of lubricating oil is also a notable characteristic. Therefore, the storage modulus ($G'$) and loss modulus ($G''$) of all plain PAOs were evaluated as functions of angular frequency and are depicted in **Figures 6.12(c)-6.12(d)**. It can be observed that all PAOs demonstrated a higher loss (viscous) modulus than storage (solid) modulus ($G'' > G'$) within the whole investigated frequency range. This implies that all PAOs can be considered as an ideal viscous liquid without any additional treatment. All PAOs exhibited the linear relationship of $G''$ with angular frequency except PAO 6, which featured that $G''$ continuously increased at lower angular frequency. On the contrary, PAO 6 revealed the linear relation of $G''$ at higher angular frequency. It is evident from **Figure 6.12(d)** that at a low shear rate, $G'$ of PAO 6 is independent of angular frequency. This range of angular frequency is called a linear viscoelastic (LVE) shear regime. Due to the high loss modulus, the lubricating oils indicate an excellent potential to form a thick tribo-film compared to lubricating oil with low loss modules. Thus, PAO 100 with high loss modulus showed best the EP properties, while PAO 4 having the lowest $G''$ exhibited worst EP characteristics than remaining PAOs, attributing to the low propensity to develop a lubricious thin film.

In addition, the Walther equation (Eq. (6.1)) was used to estimate the influence of temperature on the viscosity of PAOs, and the results are summarized in **Table 6.4**.

$$\log_{10}\log_{10}(0.7+v) = b + c\log_{10} T \quad (6.1)$$

Where $v$ is the kinematic viscosity of lubricant ($m^2/s$), $T$ is the absolute temperature (K), $b$ and $c$ are constant.

It is apparent from **Table 6.4** that the experimental viscosity values exhibited little deviation compared to the viscosity values provided by the supplier.

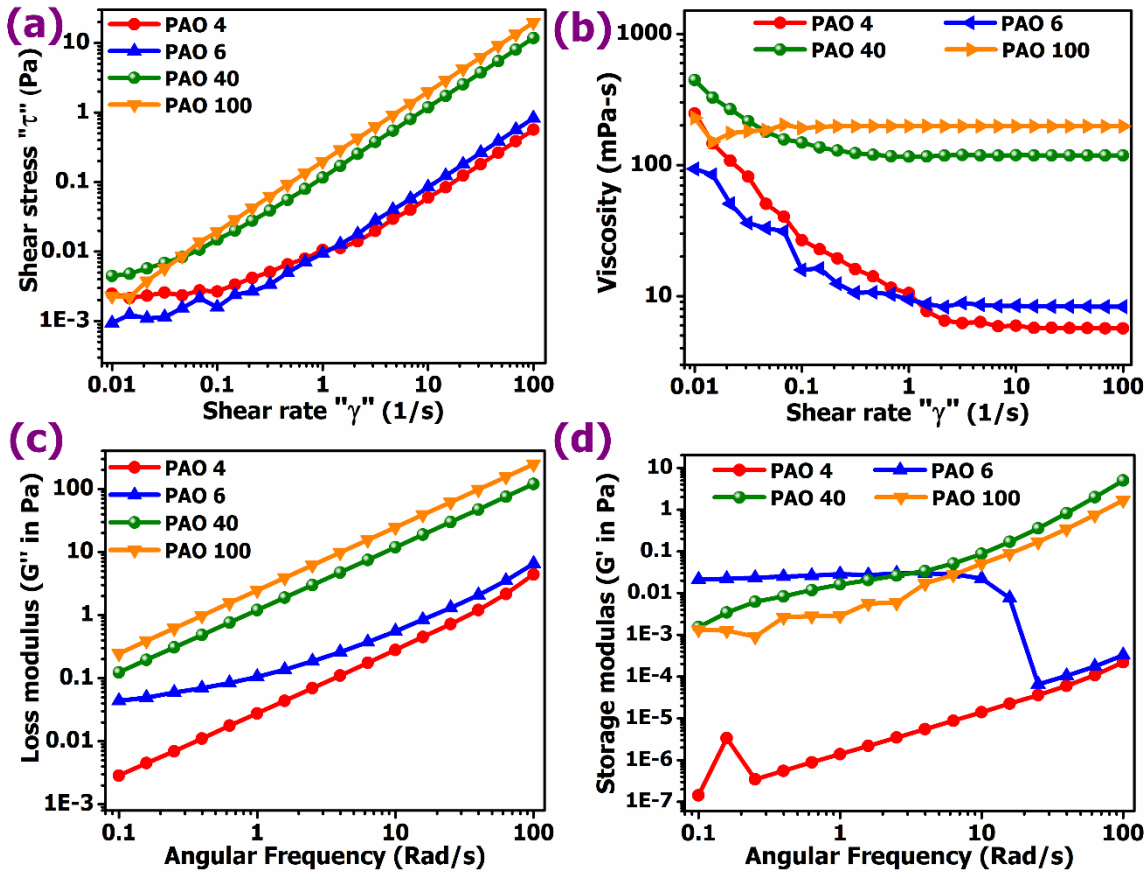


**Figure 6.12:** Rheological characterization of plain PAO 4, PAO 6, PAO 40, and PAO 100

## 6.6. Lubrication mechanism

From the above results, it can be deduced that the EP attributes of $LaF_3$ are closely related to its concentration in all PAOs. For example, at a relatively high dose of $LaF_3$, all PAOs revealed good EP properties even at higher loading conditions. Thus, it can be inferred that

the fair EP performance of $LaF_3$ at moderate loading conditions might be closely related to the physical attributes of additive. In the meantime, $LaF_3$ at high concentration in all PAOs is easier to be deposited on friction surfaces to exert a self-repairing function. Therefore, resulting in the best anti-wear performance under EP conditions. However, the anti-wear mechanism of $LaF_3$ nanoparticles can be elucidated as follows: when the lubricant film between rubbing pairs turns out to be slender, then mixed lubrication or boundary lubrication prevails (from LNSL onward), the nanoparticles may sustain a fraction of load and segregate the friction surfaces to hinder adhesion, thereby, results in enhancement in EP characteristics. However, three distinct mechanisms can occur: the first process is that the nanoparticles may be melted and fused on the interfaces of the friction surfaces, but this is impossible for the nanoparticles in the present study because their melting points are too high (i.e., 1493 ℃). The second one is that $LaF_3$ nanoparticles may be reacted with the material of the steel ball to develop a protective layer (this possibility is improbable because of the electropositive nature of $LaF_3$ nanoparticles and the material of steel balls). The last option is that nanoparticles may be tribo-sintered in the valleys of friction pairs. Therefore, it can be concluded that in the present investigation, the tribo- sintering phenomenon may be most likely occur due to the accumulation of $LaF_3$ in the grooves of friction surfaces as corroborated by SEM, SPM, and EDS results.

It may also be concluded from the results that EP properties of PAOs depend not only on the doses of $LaF_3$ but also on the viscosity. Along with additive concentrations, as the viscosity increases (i.e., from 4 cSt to 100 cSt), the EP properties of PAOs were improved. Hence, a combined effect of $LaF_3$ concentration and viscosity has been identified as an essential factor for the anti-wear ability of the PAOs under EP conditions.

**Table 6.4:** Comparison of experimental viscosity of PAOs with supplier's data

| Property | | Kinematic viscosity (ν), (cSt) | | | | | | | |
|---|---|---|---|---|---|---|---|---|---|
| | | As per supplier's | | | | Experimental | | | |
| | | PAO 4 | PAO 6 | PAO 40 | PAO 100 | PAO 4 | PAO 6 | PAO 40 | PAO 100 |
| Temperature (°C) | 40 | 19 | 31 | 396 | 1150 | 18.4 | 30.2 | 378.4 | 1132.5 |
| | 60 | 10.06 | 15.47 | 153.8 | 431.0 | 9.85 | 15.2 | 150.7 | 418.3 |
| | 80 | 6.12 | 8.98 | 72.15 | 193.6 | 6.04 | 8.9 | 71.9 | 186.1 |
| | 100 | 4.1 | 5.8 | 39 | 100 | 4.07 | 5.8 | 39.4 | 95.5 |
| Viscosity index (VI) | | 126 | 138 | 147 | 179 | 122 | 135 | 154 | 172 |

## 6.7. Summary of the chapter

This chapter adopted the sol-gel method to synthesize the $LaF_3$ nanoparticles and modified them with oleic acid (OA). The synthesized nanoparticles were characterized with various analytical tools viz. X-ray diffractometer (XRD), high-resolution transmission electron microscopy (HR-TEM), Fourier transform infrared spectroscopy (FTIR), and X-ray photoelectron spectroscopy (XPS). Two grades of low viscosity PAOs (i.e., PAO 4 and PAO 6) and two high viscosity PAOs grades (i.e., PAO 40 and PAO 100) were chosen as base oils. The varying dose (0.025-0.15 wt.%) of synthesized nanoparticles were blended in all PAOs to prepare nanolubricants. The extreme pressure (EP) properties of nanolubricants were measured using a four-ball tester as per ASTM D2783 to find the last non-seizure load (LNSL), initial seizure load (ISL), just before weld (JBWL), weld load (WL), and load wear index (LWI). The results revealed that the incorporation of $LaF_3$

nanoparticles efficiently enhanced the EP properties of all PAOs. However, 0.15 wt.% of additive was the optimum dose in all PAOs, demonstrating the best EP behaviour, i.e., the highest LWI and lowest WSD at ISL and JBWL.